Title

True phase quantitative susceptibility mapping using continuous single-point imaging: a feasibility study

Journal

Magnetic Resonance in Medicine, 81(3)

ISSN

0740-3194

Authors

Jang, Hyungseok
Lu, Xing
Carl, Michael
et al.

Publication Date

2019-03-01

DOI

10.1002/mrm.27515

Peer reviewed

Received: 7 March 2018 | Revised: 9 August 2018 | Accepted: 10 August 2018

DOI: 10.1002/mrm.27515

NOTE

Magnetic Resonance in Medicine

True phase quantitative susceptibility mapping using continuous single-point imaging: a feasibility study

Hyungseok Jang[1*] | Xing Lu[1,2*] | Michael Carl[3] | Adam C. Searleman[1] | Saeed Jerban[1] | Yajun Ma[1] | Annette von Drygalski[4] | Eric Y. Chang[1,5] | Jiang Du[1]

[1]Department of Radiology, University of California San Diego, San Diego, California

[2]Institute of Electrical Engineering, Chinese Academy of Science, Beijing, China

[3]GE Healthcare, San Diego, California

[4]Department of Medicine, Division of Hematology/Oncology, University of California, San Diego, California

[5]Radiology Service, VA San Diego Healthcare System, San Diego, California

Correspondence
Jiang Du, Department of Radiology, University of California, San Diego, 200 West Arbor Drive, San Diego, CA 92103-8226, USA.
Email: jiangdu@ucsd.edu

Funding information
NIH (1R01 NS092650, 1R01 AR068987, and T32EB005970), Veterans Affairs (Merit Award 1I01CX001388 and I01RX002604), National Natural Science Foundation of China (NSFC No. 51607169), and GE Healthcare

Purpose: In this study, we explore the feasibility of a new imaging scheme for quantitative susceptibility mapping (QSM): continuous single-point imaging (CSPI), which uses a pure phase encoding strategy to achieve true phase imaging and improve QSM accuracy.

Methods: The proposed CSPI is a modification of conventional SPI to allow acquisition of multiple echoes in a single scan. Immediately following a phase encoding gradient, the free induction decay is continuously sampled with extremely high temporal resolution to obtain k-space data at a fixed spatial frequency (i.e., at a fixed k-space coordinate). By having near-0 readout duration, CSPI results in a true snapshot of the transverse magnetization at each TE. Additionally, parallel imaging with autocalibration is utilized to reduce scan time, and an optional temporal averaging strategy is presented to improve signal-to-noise ratio for objects with low proton density or short T2* decay. The reconstructed CSPI images were input to a QSM framework based on morphology enabled dipole inversion.

Result: In an experiment performed using iron phantoms, susceptibility estimated using CSPI showed high linearity ($R^2 = 0.9948$) with iron concentration. Additionally, reconstructed CSPI phase images showed much reduced ringing artifact compared with phase images obtained using a frequency encoding strategy. In an ex vivo experiment performed using human tibia samples, estimated susceptibilities ranged from –1.6 to –2.1 ppm, in agreement with values reported in the literature (ranging from –1.2 to –2.2 ppm).

Conclusion: We have demonstrated the feasibility of using CSPI to obtain true phase images for QSM.

KEYWORDS
bone, iron, QSM, SPI, susceptibility

[*]Hyungseok Jang and Xing Lu contributed equally to this work.

1 | INTRODUCTION

Quantitative susceptibility mapping (QSM) has recently surfaced as a powerful tool to characterize pathophysiological variation of susceptibility in tissues, such as iron deposition, calcification, demyelination, and oxygenation.[1-11] QSM estimates tissue susceptibility based on phase changes in the MR signal.[12,13] Although only 1 echo is sufficient to resolve the phase evolution for QSM in general, multiecho gradient recalled echo (GRE) imaging schemes are commonly utilized to obtain accurate phase information,[14,15] where images at multiple TEs are acquired within a single or multiple acquisitions using bipolar or fly-back GRE schemes for time-efficient image acquisition. Unfortunately, in multiecho GRE imaging, echo spacing (or temporal resolution) is inherently limited by the performance of the gradient system (i.e., slew rate and maximum amplitude) to achieve the desired spatial resolution. Moreover, in bipolar multiecho GRE imaging, the phase error caused by accumulated eddy current effects needs to be corrected to achieve reliable phase information, which can be another source of error in QSM.

Non-Cartesian imaging has recently been in the limelight as an alternative to conventional Cartesian GRE imaging for QSM because of the flexible trajectories allowing for more-efficient k-space coverage.[16] In particular, ultrashort echo time (UTE) imaging techniques utilizing radial or cones trajectories have been recently proposed to enable mapping of susceptibility for tissues with short T2* decay such as cortical bone or tissues with high susceptibility.[17,18] However, linear and nonlinear distortions in the readout gradient and the resultant k-space trajectory during ramp sampling are difficult to predict and compensate for in UTE QSM. Moreover, T2* decay and phase evolution during the relatively long readout inherent in pure frequency encoding strategies (i.e., radial, cones, and spiral encoding) can result in deviations from the true magnitude and phase of the MR signal, leading to inaccurate QSM calculation.

In this study, we explore the feasibility of a new imaging technique for QSM based on single-point imaging (SPI), also known as pure phase encoding or constant time encoding, where an entire k-space is encoded at the same TE (i.e., near-0 readout duration), thus capturing a snapshot of the true phase.[19,20] Here, conventional SPI has been modified to enable continuous imaging with extremely high temporal resolution (minimum echo spacing = 2 μs in a modern clinical MR system), which we termed continuous SPI (CSPI). The proposed method allows for the time-efficient generation of images of the true phase at multiple TEs, and its application to QSM was evaluated by phantom and ex vivo experiments.

2 | METHODS

2.1 | Single-point imaging

SPI is also known as pure phase encoding or constant time imaging because of its characteristic that all k-space data are acquired at the same TE. Figure 1a shows a pulse sequence diagram for conventional SPI, where a short hard

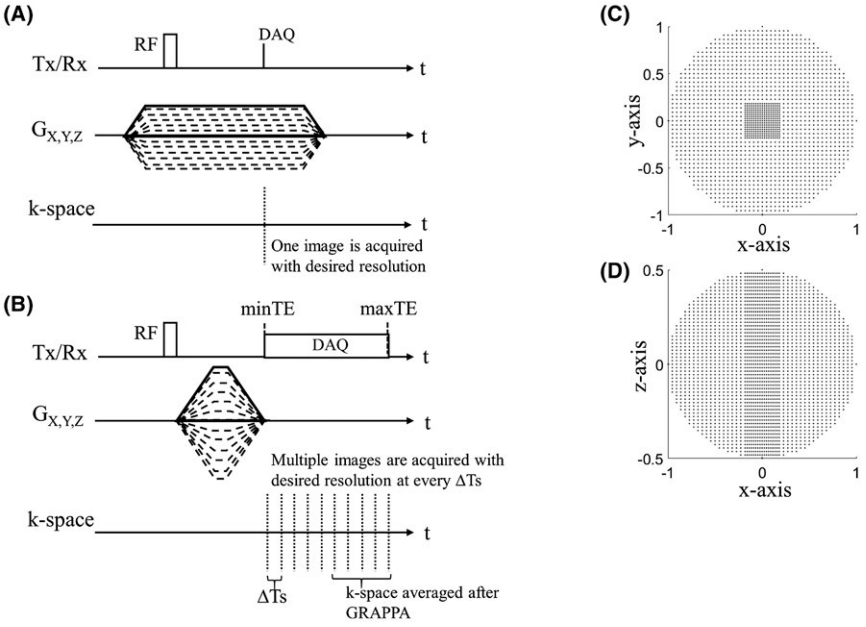

FIGURE 1 Continuous single-point imaging (CSPI). Pulse sequence diagram for (A) conventional single-point imaging and (B) proposed CSPI. An example of a spherical sampling pattern is shown for the (C) x-y axis and (D) x-z axis, with the center of k-space fully sampled and the outer k-space undersampled with reconstruction using GRAPPA. In CSPI, images with sampling interval ΔTs are continuously sampled over FID. To increase SNR, neighboring k-spaces can be temporally averaged. DAQ, data acquisition; t, encoding time

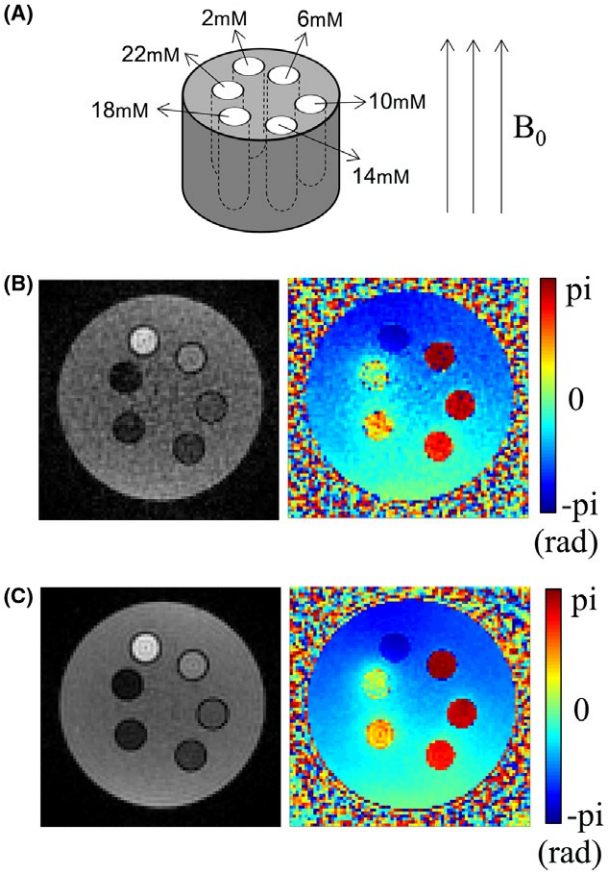

FIGURE 2 Iron phantom. (A) Phantom design, and magnitude and phase images obtained (B) before application of temporal averaging and (C) after application of temporal averaging with a window size of 32 μs. Note that in (B) and (C) temporal averaging did not distort magnitude or phase information, but significantly increased SNR. SNR was calculated using a 2-region approach, where the SNR measurement was repeated in 3 difference slices. The measured SNR was 14.7 ± 3.5 or 43.6 ± 3.0 without or with temporal averaging, respectively

pulse and a plateau of gradient are typically used for imaging. 3D SPI is performed by linearly scaling the phase encoding gradient in 3 gradient axes in each TR. To obtain SPI images at another TE, it is required to set maximum phase encoding amplitude differently and repeat image acquisition.[20] Unfortunately, this scheme is very time-intensive and hence not suitable for scenarios that require images at many TEs, such as QSM.

2.2 | Continuous single-point imaging

Figure 1b shows the pulse sequence diagram for the proposed CSPI that allows more time-efficient acquisition of multiecho images compared with conventional SPI. The proposed CSPI uses carefully designed phase encoding gradients to move to a fixed k-space coordinate (spatial frequency) followed by data acquisition at multiple TEs.

In CSPI, phase encoding gradients are rapidly ramped up after radiofrequency (RF) excitation to avoid unwanted slice selectivity artifacts as in Jang et al[21] and then switched off before data acquisition. For each sampled k-space coordinate, the phase encoding gradients are designed to have a certain area under the gradient to achieve the desired spatial resolution and minimum TE (minTE) using the following equation (Equation 1):

$$\int_0^{minTE} G(\tau)d\tau = \frac{\pi N}{\gamma FOV} \quad (1)$$

where $G(\tau)$ is the gradient amplitude at time delay τ, minTE is the time delay when the gradient is switched off and data acquisition begins, γ is the gyromagnetic ratio, FOV denotes field of view, and N denotes the matrix size. The gradient waveform of maximum phase encoding gradient used for CSPI can be designed with any shape, but a trapezoidal shape with a maximum slew rate and amplitude that hardware performance and safety factors allow with given imaging parameters was adopted in this study to achieve the shortest minimum TE. Figure 1c and 1d shows examples of 3D phase encoding steps (or spherical sampling patterns) used for the proposed CSPI. A spherical sampling pattern was adopted to reduce scan time. Moreover, GeneRalized Autocalibrating Partially Parallel Acquisitions (GRAPPA)[22] was utilized to further accelerate CSPI imaging, where central k-space is fully sampled to achieve autocalibration, and outer k-space is undersampled.

After switching off the gradients, free induction decay (FID) at a fixed k-space coordinate is continuously sampled with an extremely high temporal resolution determined by sampling interval, ΔTs, which is an inverse of readout bandwidth (BW). Data acquisition is continued until a desired maximum TE (maxTE) is achieved.

2.3 | Phantom design

To evaluate the proposed method, an iron phantom was prepared comprised of six 3-mL syringes (1 cm diameter) filled with 2 mL of Feridex I.V. solution (Berlex Laboratories, Wayne, NJ) at 6 different iron concentrations (2, 6, 10, 14, 18, and 22 mM), as shown in Figure 2a. Syringes were embedded in 0.9% weight/volume agarose gel in a plastic cylinder (10 cm diameter, 30 cm height). In addition, an ex vivo sample was prepared consisting of 3 cadaveric cortical tibia midshaft bones. Bone samples were harvested from 3 deceased individuals (38-year-old female, 49-year-old female, and 53-year-old male at death) provided by a nonprofit whole-body donation company (United Tissue Network, Phoenix, AZ). Samples were cut to 25 mm in length using a Delta ShopMaster band saw (Delta Machinery, Jackson, TN), then the bone marrow

was removed gently using a scalpel. Bone samples were put into 0.9% weight/volume agarose gel in a plastic container with the same dimensions as the iron phantom.

2.4 | Imaging parameters

The iron phantom and human bone samples were imaged at 3T (MR750; GE Healthcare, Waukesha, WI) using a 16-channel receive-only wrap coil (NeoCoil, Pewaukee, WI), with the longitudinal direction of the tubes or bones placed parallel to the B_0 field. CSPI was performed using the following imaging parameters: RF = 100 μs hard pulse, flip angle (FA) = 6°, slew rate = 200 mT/m/msec, voxel size = 1 × 1 × 2 mm, FOV = 81 × 81 × 110 mm^3, acceleration factor for parallel imaging = 2 × 2 × 1, matrix size for autocalibration = 17 × 17 × 55, readout BW = ±250 kHz, ΔTs = 2 μs, reconstructed TE = 504, 536, …, 2008 μs (total 48 TEs), TR = 5 ms, and scan time = 4 minutes 45 seconds. Note that system maximum readout BW (±250 kHz) was applied to achieve the highest temporal resolution with the shortest echo spacing (2 μs). After GRAPPA reconstruction, temporal averaging with a window size of 32 μs was applied, where the window size was empirically found to achieve enough signal-to-noise ratio (SNR) on the cortical bone samples and the highest concentration iron phantom. For comparison, a 3D-Cones[18,23] image was obtained with RF pulse, FOV, voxel size, TR, and FA matched to CSPI and with the following imaging parameters: readout BW = ±83.3 kHz, TE = 32, 132, 232, 432, 532, 632, 732, and 832 μs, total scan time = 7 minutes 20 seconds.

2.5 | Image reconstruction

All CSPI images were reconstructed utilizing 3D GRAPPA reconstruction using a kernel size of 5 × 5 × 7 pixels. After GRAPPA reconstruction, data acquired by individual phased array channels were combined using an adaptive reconstruction method.[24] Consequently, a series of complex MR images is obtained between minTE and maxTE with an extremely high temporal resolution (echo spacing of ΔTs). Unfortunately, SNR in the images is decreased because of parallel imaging depending on the acceleration factor and a geometry factor, which can be problematic when imaging subjects with short T2* decay (e.g., connective tissues such as bone or tissues with high susceptibility). To enhance SNR in CSPI, consecutive k-spaces within a small TE window are temporally averaged, as illustrated in Figure 1b, under the assumption that the change in phase or magnitude within the small range of TE is negligibly small. The temporal averaging step is optional and not necessary when objects with high signal intensity are imaged.

2.6 | QSM analysis

For the calculation of susceptibilities, morphology enabled dipole inversion (MEDI)-based QSM reconstruction was applied offline.[12] A 4D complex matrix of CSPI images in order of increasing TE, along with masking of the cylinder phantom and calculation of the B_0 direction from localization information, were used for input into the MEDI algorithm. The first 12 of 48 total reconstructed CSPI images (TE = 504, 536, …, 856 μs) were used for estimating the frequency shift in an iterative fashion. For 3D-Cones, all 8 images were used for QSM analysis. A region-growing–based phase unwrapping algorithm was implemented to obtain the global frequency shift.[25] The Projection onto Dipole Fields algorithm was used to remove the background from the frequency shift and phase map.[26] Dipole inversion of the local susceptibility distribution was realized using an iterative Bayesian regulation method.[12] The regularization parameter was set to 500 for the iron phantom and 200 for the bone samples.

3 | RESULTS

3.1 | Iron phantom experiment

Figure 2b and 2c shows magnitude and phase of CSPI images of the iron phantom at TE = 536 μs before and after application of temporal averaging of neighboring k-spaces. Averaging 17 images with a window size of 32 μs significantly improved SNR without notable distortion of magnitude or phase information. Measured SNR at the area of agarose gel in the magnitude image was 14.7 ± 3.5 and 43.6 ± 3.0 for CSPI images without and with the temporal averaging, respectively.

Figures 3a shows phase images of the iron phantom at 12 different TEs in CSPI. Figure 3b shows phase maps in the same location acquired by 3D-Cones or CSPI at a representative matched TE (0.5 ms). In the 3D-Cones image, blurriness and inhomogeneity near tubes (black arrows) are observed in the phase map, presumably attributed to off-resonance effects (or field shift) during frequency encoding with long readout duration (1.2 ms), whereas CSPI (pure phase encoding) is less affected by the off-resonance effect attributed to near-0 readout duration.

Figure 4a shows the MEDI-based QSM results of the iron phantom using 3D-Cones or CSPI, and Figure 4b shows ordinary least-squares fitted curves of the estimated susceptibility over different iron concentrations. With the 3D-Cones, mean and standard deviation of the estimated susceptibility in each tube were 1.2 ± 1.1, 9.5 ± 1.3, 18.1 ± 3.5, 23.6 ± 4.5, 32.9 ± 5.6, or 36.7 ± 10.2 ppm, respectively. The estimated mean susceptibility showed high linearity ($R^2 = 0.9906$) with the fitted equation for susceptibility, $\chi_{3D\text{-}Cones} = 1.8[Fe] - 1.4$ (ppm). With the CSPI, mean and standard deviation of the estimated susceptibility in each tube were 3.1 ± 0.8, 10.2 ± 0.9, 16.6 ±

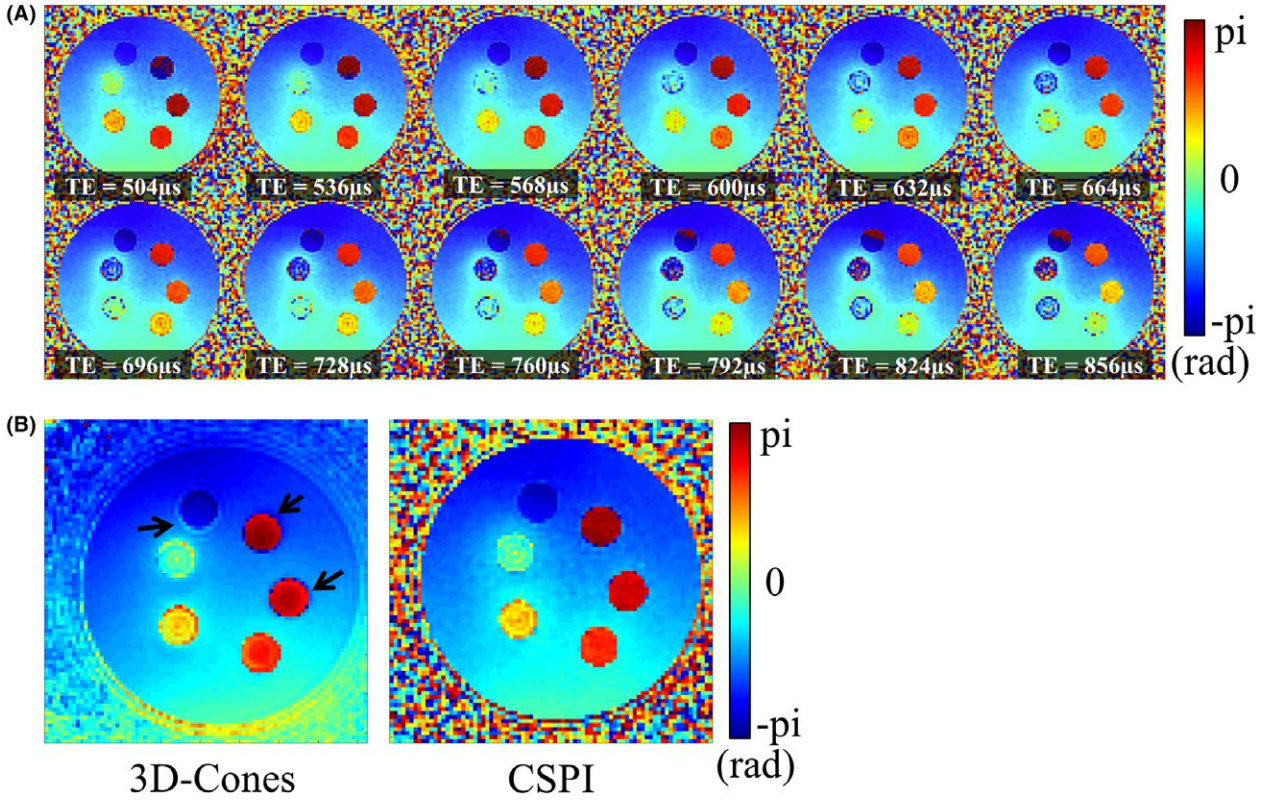

FIGURE 3 Reconstructed images for iron phantom QSM. (A) Phase images in CSPI and (B) comparison between phase images from 3D-Cones and CSPI at TE = 0.5 ms. The tubes with high iron concentrations have more prominent off-resonance susceptibility in the phase image obtained using 3D-Cones, as indicated by the black arrows, presumably attributed to the long frequency encoding readout (1.2 ms) that is more prone to off-resonance effects

2.5, 22.3 ± 2.0, 28.9 ± 3.3, or 32.9 ± 3.0 ppm, respectively. The estimated mean susceptibility showed high linearity (R^2 = 0.9948) with the fitted equation for susceptibility, χ_{CSPI} = 1.5[Fe] + 1.0 (ppm). The susceptibility map obtained by CSPI shows significantly reduced spatial distortion than that by 3D-Cones, owing to the robustness to off-resonance effect. The estimated susceptibilities show a discrepancy, especially for the tubes with high iron concentrations, which is presumably attributed to the different minimum TEs in CSPI and 3D-Cones given that UTE-QSM can be affected by selection of TEs.[18]

3.2 | Ex vivo bone sample experiment

Figure 5b shows the phase of reconstructed CSPI images for the human tibia bone samples. As seen, magnitude and phase signals in bone regions remain well above noise levels over a range of TEs. Figure 5b shows the estimated susceptibility map using the 12 CSPI images. Susceptibilities in regions of interest (ROIs) #1, #2, and #3 were –2.1 ± 0.02, –1.9 ± 0.03, and –1.6 ± 0.02 ppm, respectively, which are similar to the reported values for cortical bone in the literature, which ranges from –1.2 to –2.2 ppm.[17,27] High susceptibility noted near the endosteal surface was presumed to be from residual bone marrow.

4 | DISCUSSION

In this study, we explored the feasibility of CSPI for robust and efficient QSM. In conventional imaging schemes for QSM, different parts of k-space are encoded at different time delays because of the readout length, during which phase evolution continues. As a result, phase information in the MR image can deviate from the true phase. In contrast, SPI provides truly accurate phase information owing to the pure phase encoding scheme where each k-space coordinate is encoded at the same TE. In contrast to conventional SPI, the CSPI method allows for obtaining multiple echoes at a given k-space coordinate in a single acquisition. In the iron phantom experiment, we have shown that CSPI achieves highly accurate QSM with high linearity of the estimated susceptibility over a wide range of iron concentrations. We have also shown that CSPI is robust to the off-resonance effects that are observed using 3D-Cones UTE (Figure 3c). Additionally, the ex vivo human cortical bone sample experiment demonstrated the feasibility of CSPI-based QSM, with consistent cortical bone susceptibility values that are similar to reported values: –1.6 to –2.1 ppm by CSPI compared to –1.2 to –2.2 ppm from the literature.[17,24]

The proposed CSPI has many advantages over conventional SPI. First, CSPI is highly time-efficient compared with conventional SPI. For example, in this study, 816 images were reconstructed using CSPI within a single scan, which is 816× faster encoding compared with the conventional SPI where a single image is acquired within a single scan. The high temporal resolution images were utilized to improve SNR by temporal averaging over short temporal windows, which significantly increased SNR. This can be especially beneficial when imaging a subject with short T2* decay such as bone. Moreover, the temporal averaging with data acquired in high BW allows flexibility to adjust temporal resolution at the stage of image reconstruction. For example, if a targeted subject shows high enough SNR in the reconstructed image, less-temporal averaging can be applied to achieve higher temporal resolution, and vice versa. Another possible strategy is performing temporal averaging in a sliding window scheme, which can enhance SNR with high temporal resolution preserved. Note that this temporal averaging is not available in conventional SPI because neighboring k-spaces have different FOVs (or different sampling intervals) because of the effective gradients.[28] The applications in which a short hard pulse is necessary (e.g., metal imaging)[29] will benefit from CSPI with temporal averaging.

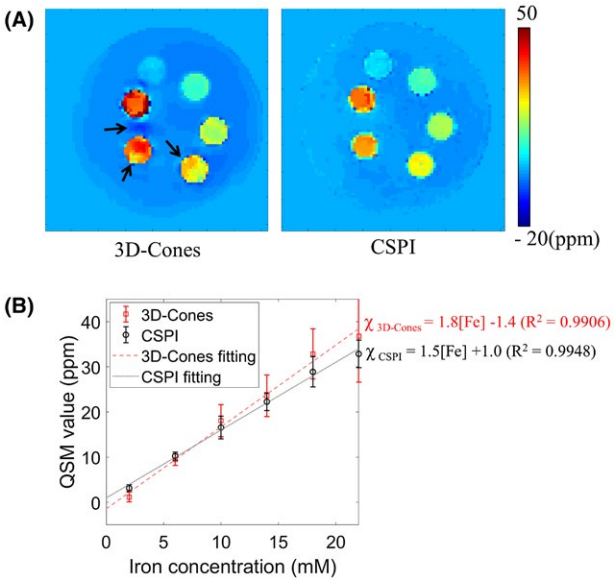

FIGURE 4 Estimated QSM for the iron phantom. (A) QSM map with 3D-Cones and CSPI and (B) fitted curves. The estimated susceptibility map with CSPI shows less spatial distortion compared to that with 3D-Cones, owing to the near-0 readout duration, which is robust to the off-resonance effect. The curve fitting shows high linearity in CSPI-based QSM

One limitation of CSPI is that the minimum TE is determined by the desired spatial resolution and the performance of the gradient system (i.e., slew rate and amplitude). Although we have shown that CSPI can accurately estimate the susceptibility of cortical bone in this study, the minimum TE at around 0.5 ms is relatively long for UTE imaging, where minimum TEs below 0.1 ms are commonly used in order to maximize signal from short T2* tissues. However, the proposed CSPI can be further modified to shorten the minimum TE by incorporating more-advanced techniques, such as k-space extrapolation, where high-frequency k-space data are shared between different TEs to secure images before the minimum TE.[28] Another approach is to use variable TE where the low-frequency data can be acquired with shorter TEs because smaller phase encoding gradient moments are needed, whereas the high-frequency data can be acquired with longer TEs because larger phase encoding gradient moments are needed.[30]

Another limitation of CSPI is that the scan time increases with FOV. For example, n-times larger FOV in 1 gradient axis will require n-time higher sampling density (number of TRs) to avoid aliasing (or fold-over) artifacts. Therefore, accelerated imaging is crucial for CSPI to be clinically useful. Restricting the effective FOV would be a simple strategy to accelerate CSPI, for instance, by using coils with small volume and sensitivity (e.g., surface coils) or applying slab selection, for example, by using a half pulse or Shinnar–Le

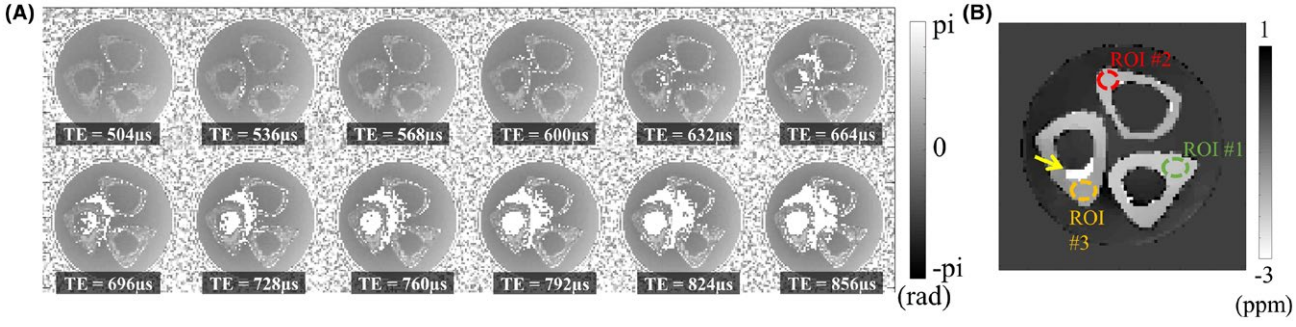

FIGURE 5 QSM of cadaveric human tibia samples. (A) Phase images obtained using CSPI, and (B) estimated bone QSM. In (B) Susceptibilities in ROIs #1, #2, and #3 were –2.1 ± 0.02, –1.9 ± 0.03, and –1.6 ± 0.02 ppm, respectively. Note that in (B) residual bone marrow distorted the susceptibility, as indicated by the yellow arrow

Roux pulse with minimum phase.[31,32] Furthermore, a 3D non-Cartesian sampling pattern with variable density can be used to produce noise-like aliasing patterns that can be removed by postprocessing, such as denoising or compressed sensing techniques.[33,34] With any of the above strategies for accelerating CSPI, the key advantageous feature of CSPI, true phase imaging, will be still preserved. In future studies, we will explore the aforementioned strategies more rigorously to evaluate CSPI in clinical applications, including patients with metallic implants or hemophilia.

In this study, we have shown CSPI acquisition used for UTE-QSM analysis (i.e., iron deposition and bone susceptibility), but the proposed CSPI could also be used for general QSM applications, including for tissues with longer T2* such as brain. The longer TR required to acquire later TEs for these applications would increase scan time, which could be compensated for by using the above-mentioned acceleration strategies. Moreover, CSPI can be used for other quantitative imaging methods, which would benefit from true phase continuous TE imaging, such as fat quantification.

5 | CONCLUSION

In this study, we have shown feasibility of a new imaging scheme, continuous single-point imaging, which allows capture of the true phase information at a desired TE with extremely high temporal resolution for more-accurate quantitative susceptibility mapping.

REFERENCES

1. Barbosa JH, Santos AC, Tumas V, et al. Quantifying brain iron deposition in patients with Parkinson's disease using quantitative susceptibility mapping, R2 and R2*. *Magn Reson Imaging*. 2015;33:559–565.
2. Acosta-Cabronero J, Betts MJ, Cardenas-Blanco A, Yang S, Nestor PJ. In vivo MRI mapping of brain iron deposition across the adult lifespan. *J Neurosci*. 2016;36:364–374.
3. Chen W, Zhu W, Kovanlikaya I, et al. Intracranial calcifications and hemorrhages: characterization with quantitative susceptibility mapping. *Radiology*. 2014;270:496–505.
4. Straub S, Laun FB, Emmerich J, et al. Potential of quantitative susceptibility mapping for detection of prostatic calcifications. *J Magn Reson Imaging*. 2017;45:889–898.
5. Wisnieff C, Ramanan S, Olesik J, Gauthier S, Wang Y, Pitt D. Quantitative susceptibility mapping (QSM) of white matter multiple sclerosis lesions: interpreting positive susceptibility and the presence of iron. *Magn Reson Med*. 2015;74:564–570.
6. Chen W, Gauthier SA, Gupta A, et al. Quantitative susceptibility mapping of multiple sclerosis lesions at various ages. *Radiology*. 2014;271:183–192.
7. Langkammer C, Liu T, Khalil M, et al. Quantitative susceptibility mapping in multiple sclerosis. *Radiology*. 2013;267:551–559.
8. Wen Y, Nguyen TD, Liu Z, et al. Cardiac quantitative susceptibility mapping (QSM) for heart chamber oxygenation. *Magn Reson Med*. 2018;79:1545–1552.
9. Fan AP, Bilgic B, Gagnon L, et al. Quantitative oxygenation venography from MRI phase. *Magn Reson Med*. 2014;72:149–159.
10. Zhang J, Liu T, Gupta A, Spincemaille P, Nguyen TD, Wang Y. Quantitative mapping of cerebral metabolic rate of oxygen (CMRO 2) using quantitative susceptibility mapping (QSM). *Magn Reson Med*. 2015;74:945–952.
11. Xu B, Liu T, Spincemaille P, Prince M, Wang Y. Flow compensated quantitative susceptibility mapping for venous oxygenation imaging. *Magn Reson Med*. 2014;72:438–445.
12. de Rochefort L, Liu T, Kressler B, et al. Quantitative susceptibility map reconstruction from MR phase data using bayesian regularization: validation and application to brain imaging. *Magn Reson Med*. 2010;63:194–206.
13. Wang Y, Liu T. Quantitative susceptibility mapping (QSM): decoding MRI data for a tissue magnetic biomarker. *Magn Reson Med*. 2015;73:82–101.
14. Li J, Chang S, Liu T, et al. Phase-corrected bipolar gradients in multi-echo gradient-echo sequences for quantitative susceptibility mapping. *Magn Reson Mater Phys Biol Med*. 2015;28:347–355.
15. Liu T, Surapaneni K, Lou M, Cheng L, Spincemaille P, Wang Y. Cerebral microbleeds: burden assessment by using quantitative susceptibility mapping. *Radiology*. 2012;262:269–278.
16. Stäb D, Bollmann S, Langkammer C, Bredies K, Barth M. Accelerated mapping of magnetic susceptibility using 3D planes-on-a-paddlewheel (POP) EPI at ultra-high field strength. *NMR Biomed*. 2017;30:e3620.
17. Dimov AV, Liu Z, Spincemaille P, Prince MR, Du J, Wang Y. Bone quantitative susceptibility mapping using a chemical species-specific R2* signal model with ultrashort and conventional echo data. *Magn Reson Med*. 2018;79:121–128.
18. Lu X, Ma Y, Chang EY, et al. Simultaneous quantitative susceptibility mapping (QSM) and R2* for high iron concentration quantification with 3D ultrashort echo time sequences: an echo dependence study. *Magn Reson Med*. 2018;79:2315–2322.
19. Emid S, Creyghton JH. High resolution NMR imaging in solids. *Phys B*. 1985;128:81–83.
20. Subramanian S, Devasahayam N, Murugesan R, Yamada K, Cook J, Taube A, Mitchell JB, Lohman JAB, Krishna MC. Single-point (constant-time) imaging in radiofrequency Fourier transform electron paramagnetic resonance. *Magn Reson Med*. 2002;48:370–379.
21. Jang H, Wiens CN, McMillan AB. Ramped hybrid encoding for improved ultrashort echo time imaging. *Magn Reson Med*. 2016;76:814–825.
22. Griswold MA, Jakob PM, Heidemann RM, et al. Generalized autocalibrating partially parallel acquisitions (GRAPPA). *Magn Reson Med*. 2002;47:1202–1210.
23. Gurney PT, Hargreaves BA, Nishimura DG. Design and analysis of a practical 3D cones trajectory. *Magn Reson Med*. 2006;55:575–582.
24. Walsh DO, Gmitro AF, Marcellin MW. Adaptive reconstruction of phased array MR imagery. *Magn Reson Med*. 2000;43:682–690.
25. Cusack R, Papadakis N. New robust 3-D phase unwrapping algorithms: application to magnetic field mapping and undistorting echoplanar images. *Neuroimage*. 2002;16:754–764.

26. Liu T, Khalidov I, de Rochefort L, et al. A novel background field removal method for MRI using projection onto dipole fields (PDF). *NMR Biomed*. 2011;24:1129–1136.
27. De Rochefort L, Brown R, Prince MR, Wang Y. Quantitative MR susceptibility mapping using piece-wise constant regularized inversion of the magnetic field. *Magn Reson Med*. 2008;60:1003–1009.
28. Jang H, Subramanian S, Devasahayam N, et al. Single acquisition quantitative single-point electron paramagnetic resonance imaging. *Magn Reson Med*. 2013;70:1173–1181.
29. Wiens CN, Artz NS, Jang H, McMillan AB, Koch KM, Reeder SB. Fully phase-encoded MRI near metallic implants using ultrashort echo times and broadband excitation. *Magn Reson Med*. 2018;79:2156–2163.
30. Song HK, Wehrli FW. Variable TE gradient and spin echo sequences for in vivo MR microscopy of short T2 species. *Magn Reson Med*. 1998;39:251–258.
31. Horch RA, Wilkens K, Gochberg DF, Does MD. RF coil considerations for short-T2 MRI. *Magn Reson Med*. 2010;64:1652–1657.
32. Jang H, Liu F, Bradshaw T, McMillan AB. Rapid dual-echo ramped hybrid encoding MR-based attenuation correction (dRHE-MRAC) for PET/MR. *Magn Reson Med*. 2018;79:2912–2922.
33. Jang H, Matsumoto S, Devasahayam N, et al. Accelerated 4D quantitative single point EPR imaging using model-based reconstruction. *Magn Reson Med*. 2015;73:1692–1701.
34. Lustig M, Donoho D, Pauly JM. Sparse MRI: the application of compressed sensing for rapid MR imaging. *Magn Reson Med*. 2007;58:1182–1195.

How to cite this article: Jang H, Lu X, Carl M, et al. True phase quantitative susceptibility mapping using continuous single-point imaging: a feasibility study. *Magn Reson Med*. 2019;81:1907–1914. https://doi.org/10.1002/mrm.27515